American Mineralogist, Volume 88, pages 713–724, 2003

TEM study of mullite growth after muscovite breakdown

CARLOS RODRIGUEZ-NAVARRO,* GIUSEPPE CULTRONE, ANTONIO SANCHEZ-NAVAS, AND EDUARDO SEBASTIAN

Departamento de Mineralogía y Petrología, Universidad de Granada, Fuentenueva s/n, 18002 Granada, Spain

ABSTRACT

Mullite (Mul) formation after high-*T* muscovite (Ms) breakdown has been studied in phyllosilicate-rich bricks. At $T \geq 900$ °C Ms dehydroxylation is followed by partial melting that triggers the nucleation and growth of Mul acicular crystals. An analytical electron microscopy study reveals that the Mul is a 3:2-type with a $^{[6]}(Al_{1.686}Ti_{0.031}Fe_{0.159}Mg_{0.134})^{[4]}(Al_{2.360}Si_{1.649})O_{9.82}$ formula and an O atom vacancy of $x = 0.18$. This is consistent with X-ray diffraction results [i.e., unit-cell parameters: $a = 7.553(7)$, $b = 7.694(7)$, and $c = 2.881(1)$ Å, $V = 167.45$ Å^3]. The initial stage of the process resulting in Mul growth followed the balanced reaction $Ms \rightarrow 0.275Mul + 0.667Melt + 0.244K_2O + 0.01Na_2O + 0.125H_2O$, yielding an alkali-poor peraluminous melt. H_2O with K (and Na), which are lost along the (001) planes of dehydroxylated Ms, play a significant role as melting agents. The **c**-axes of the Mul crystals are oriented parallel to $[010]_{ms}$ or to the symmetrically equivalent $<310>_{ms}$ zone axis, while the $(120)_{mul}$ or $(210)_{mul}$ planes are subparallel to $(001)_{ms}$ (TEM results). These systematic orientations point to epitaxial Mul nucleation and growth on the remaining Ms substrate, which acts as a template for Mul heterogeneous nucleation. Randomly oriented Mul growth is also observed during the late stages of the process (i.e., melt cooling). The epitaxial nature of Mul growth after dehydroxylated Ms melting minimizes the energy requirement for nucleation. In addition, the water released after Ms breakdown and the multicomponent nature of the melt enable this high-*T* aluminum silicate to grow at $T \sim 900$ °C, almost 100 °C below the SiO_2-Al_2O_3-K_2O ternary system eutectic (after a melt with an end-member Ms composition).

INTRODUCTION

Low-pressure, high-temperature phyllosilicate transformation has been of interest to the scientific community for decades. Such interest is due both to its importance in the geosciences (e.g., pyrometamorphism) and to its technological implications in ceramic processing and in new materials design.

The micas are among the most abundant phyllosilicates of clayey raw materials used in the ceramic industry (Barlow and Manning 1999). Within this group, it has been reported that muscovite (Ms) undergoes significant changes upon heating at $T > 350$ °C (Vassányi and Szabó 1993). First, dehydroxylation takes place through the gradual loss of OH groups (Gaines and Vedder 1964). Ms is fully decomposed at $T \sim 950$ °C (Peters and Iberg 1978) and is transformed into one or a series of phases including Kfs, Qtz, Mul, Sil, Crn, Spl, and/or Lct (mineral symbols after Kretz 1983) plus a glass (Roy 1949; Sundius and Byström 1953; Eberhart 1963; Grapes 1986; Brearley and Rubie 1990; Barlow and Manning 1999; Mazzucato et al. 1999). However, there is little consensus regarding how and at what *T* these transformations take place (Barlow and Manning 1999).

Many authors have described the presence of the aluminum silicate mullite (Mul) in Ms-rich materials following high-*T* processes: e.g., in pyrometamorphic rocks (Grapes 1986; Brearley 1986; Worden et al. 1987; Clark and Peacor 1992) and in ceramics (Sundius and Byström 1953; Schmücker et al. 1995; Cultrone et al. 2001). Researchers have proposed several Ms-out reactions resulting in Mul formation, either alone or together with a wide range of silicate phases (Schairer and Bowen 1947; Sundius and Byström 1953; Grapes 1986; Brearley and Rubie 1990). Sundius and Byström (1953) and Eberhart (1963) observed that some needle-shaped Mul crystals formed after Ms breakdown were arranged in a hexagonal pattern. Using X-ray diffraction data of Mul formed after Ms dehydroxylation, Eberhart (1963) concluded that $[001]_{mul}$ directions were always parallel to Ms octahedral chains, thus suggesting that Mul formation after Ms was somehow structurally controlled/related. However, Eberhart's pioneering study gives no conclusive explanation for this observation.

Transmission electron microscopy (TEM) has been used to observe high-*T* Ms texture and phase relations (Brearley 1986; Worden et al. 1987; Brearley and Rubie 1990; Clark and Peacor 1992), since it offers the highest possible resolution for the study of layered silicates and their transformations (Baronnet 1997). TEM enables detailed high-magnification studies of phase transitions and this is particularly relevant in those rare cases in which reactants and products are preserved, as in pyrometamorphic rocks (Brearley 1986).

By using TEM, Brearley (1986) and Worden et al. (1987) were able to observe how a melt and Mul (alone or associated with Qtz and Kfs) appeared within dehydroxylated Ms crystals. Worden et al. (1987) found that some orientation relationships between the original mica (a phengite) and the reaction products (i.e., Mul) were similar to those described by Eberhart (1963). However, no detailed crystallographic studies of the

* E-mail: carlosrn@ugr.es

relationship between the two phases have been performed and, therefore, no decisive clues regarding the transformation mechanism presently exist.

In the present study, TEM has been used to determine the mechanism of Mul formation after high-*T* Ms breakdown in Ms-rich ceramic bricks fired at different *T* (700–1100 °C). This research enables a detailed analysis of both the different stages in the Ms to Mul reaction and the structural (crystallographic) relationships among the precursor and product phases. This may help us gain a more thorough understanding of the transformation process.

MATERIALS AND METHODS

Brick samples were fashioned in wooden moulds (24.5 × 11.5 × 4 cm) after mixing water with a phyllosilicate-rich clay (Guadix, Spain) traditionally used in ceramics. Samples were fired in an air-ventilated electric oven (Herotec, CR-35) at different temperatures, ranging from 700 to 1100 °C. *T* was increased at a rate of 3 °C per minute, first up to 100 °C with one hour soaking time, and later up to the peak *T* with a soaking time of three hours. Finally, the oven was turned off and samples were left to cool inside for 24 hours. *T* decay was exponential during cooling, with a cooling rate of close to 6 °C per minute in the 1000–600 °C interval. The oven *T* control was calibrated using substances whose melting points are well-known (KI, at 682 °C, KCl, at 770 °C, NaCl, at 800 °C, Na_2CO_3, at 851 °C, Na_2SO_4, at 884 °C, and NaF, at 980 °C). *T* errors were on the order of ±5 °C in the 700–1000 °C interval. The firing protocol was set to mimic standard industrial brick firing procedures (additional details on sample preparation and processing, as well as firing protocol, can be found in Cultrone et al. 2001). Phase analyses of the clay-rich raw material and the bricks were performed by powder X-ray diffraction (XRD) using a Philips PW-1710 diffractometer with an automatic slit, Cu*K*α radiation (λ = 1.5405 Å), 3 to 60° 2θ range, with steps of 0.028° 2θ and 0.01° 2θ s^{-1} goniometer speed. Mul cell parameters (*a*, *b*, and *c*) were determined from the six most intense Bragg peaks (i.e., 110, 120, 210, 220, 111, and 121) using the PLV unit-cell refinement program (Martin Ramos 1990). It was not possible to use more Mul reflections because of the presence of other phases that masked the less intense reflections. Although the cell parameter uncertainties are somewhat high, cell values are considered appropriate for Mul compositional analysis using data from Cameron (1977).

Uncovered Canadian balsam-mounted thin sections of brick samples fired at 800, 900, and 1000 °C were prepared and polished. Following preliminary optical microscopy analyses, large (up to 1 mm long) selected Ms crystals were studied by means of TEM (Philips CM20), operated at a 200 kV acceleration voltage and equipped with an EDAX solid-state energy-dispersive X-ray detector with an ultra-thin window (UTW). The objective aperture was 40 μm, which represents a compromise between amplitude and phase contrast images. Lattice images with $d_{hkl} > 0.4$ nm were collected in this way. Quantitative analytical electron microscopy (AEM) of Ms and high-*T* phases (Mul and melt) was performed only on thin edges in scanning TEM (STEM) mode (<400 counts s^{-1}) using a 4 nm diameter beam and a 100 × 20 nm scanning area. A low background condenser aperture and an analytical Be sample holder were employed to improve spectrum quality. Ms, Ab, Bt, Sps, Ol, and Ttn standards were used to obtain *k*-factors ($k_{x/Si}$) allowing X-ray intensities to be corrected by the thin-film method (Cliff and Lorimer 1975; Champness et al. 1981), as modified by Mellini and Menichini (1985) for AEM analysis of silicate minerals. Average errors for analyzed elements (two standard deviations) expressed as a percentage of the atomic proportions are 6 (Na), 3 (Mg), 2 (Al), 4 (K), 4 (Ca), 5 (Ti), 3 (Mn), and 3 (Fe). Errors due to K loss during AEM analysis were corrected by determining K concentration at 30 and 200 s beam-exposure time, and scaling K concentration back to zero seconds as described by Worden et al. (1987). Prior to TEM observations, the selected Ms crystals were removed from the thin sections, were further thinned using a Gatan 600 ion-mill, and were finally coated with carbon (as in Barber 1970).

Polished thin sections of brick samples fired at 700, 1000, and 1100 °C were carbon-coated, and Si, K, and Al distribution X-ray images, as well as back-scattered electron (BSE) images of Ms and Mul grains, were obtained with a Cameca SX50 electron probe microanalyzer (EPMA) fitted with a Link Systems wavelength-dispersive spectrometer (WDS). Quantitative analyses of selected Ms grains (and high-*T* pseudomorphs) were also performed using this technique. The EPMA working conditions were 20 keV beam energy, 0.7 mA filament current, and 2 μm spot-size diameter. Ab, Or, Per, Wo, and oxides (Al_2O_3, Fe_2O_3, and $MnTiO_2$) were used as standards. Full ZAF corrections were applied to all data.

Thermogravimetric analyses (TGA, Shimadzu TGA-50H) of raw brick clay-rich material were performed to understand how water loss, i.e., dehydroxylation, took place upon sample firing. TGA was performed in a flush-air atmosphere (100 mL/min), using aluminum cells, a heating rate of 5 °C/min, and an interval of 25–950 °C. On-line coupled infrared (IR) and mass spectrometry (MS) were used together with TGA for evolved-gas analysis.

RESULTS

XRD analysis

Table 1 shows the mineralogical composition of the raw material and the bricks fired at the above-mentioned *T*, as inferred from XRD. Details on brick sample bulk mineralogy and its evolution upon firing have been published elsewhere (Cultrone et al. 2001). XRD analysis showed that the Ms was a $2M_1$ polytype (Barlow and Manning 1999). Mul was clearly

TABLE 1. XRD phase analysis of brick samples fired at different *T*

Firing *T*	Qtz	Phy	Hem	Mul	Fs
Raw material	*	*	‡	nd	‡
700 °C	*	*	nd	nd	‡
800 °C	*	†	‡	nd	‡
900 °C	*	†	‡	nd	‡
1000 °C	*	nd	‡	‡	‡
1100 °C	*	nd	‡	†	‡

Notes: nd = not detected; phy = phyllosilicates, mainly Ms and Ill with traces of Kao and smectite. Mineral symbols after Kretz (1983).
* Very abundant.
† Abundant.
‡ Scarce.

detected in bricks fired at $T \geq 1000$ °C. It should be mentioned that XRD is not a very accurate technique for identifying phases in concentrations <5 wt%. Therefore it is not known if Mul was already present in the bricks fired at 900 °C (or lower T). TEM offers a more conclusive answer to the minimum T for Mul formation, as will be seen below. XRD data showed that the Mul lattice parameters are: $a = 7.553(7)$ Å, $b = 7.694(7)$ Å and $c = 2.881(1)$ Å, $Z = 1$, unit-cell volume = 167.45 Å^3, corresponding to a $3Al_2O_3.2SiO_2$ or 3:2-Mul variety (Agrell and Smith 1960; Cameron 1977). It is a silica-rich Mul, with a theoretical structural formula $^{[6]}Al_2{}^{[4]}(Al_{2+2x}Si_{2-2x})O_{10-x}$ (Aksay et al. 1991), where x (i.e., the number of O atoms missing per unit cell) has a value of ~0.25 (x value calculated using unit-cell parameters after Cameron 1977).

Thermal analysis

TGA results (Fig. 1) show a step-wise weight loss with a slightly decreasing rate in the 500–750 °C interval. The weight-loss rate was significantly lower from 750 °C to 950 °C. On-line IR and MS analyses confirmed that H_2O was the only gas released at $T > 500$ °C. Trace amounts of CO_2 from organic matter were detected at lower temperatures. Sample dehydration was not complete at maximum T, indicating that some OH groups remained in the dehydroxylating phyllosilicates. In addition to Ms, bulk samples also contained a significant amount of clays (Ill with traces of smectite and Kln; see Cultrone et al. 2001) that may have enhanced water loss at $T < 550$ °C (Fig. 1). Dehydroxylation of these minerals is complete at 500–600 °C (Brindley and Nakahira 1959; Deer et al. 1982); they do not thus significantly contribute to the weight loss shown at $T >$ 600 °C. These results suggest that Ms dehydroxylation is a step-wise process, incomplete (within the time-scale of our experiment) at 950 °C, as has also been shown by other studies (Eberhart 1963; Guggenheim et al. 1987; Barlow and Manning 1999). According to Velde (1966), the equilibrium temperature for Ms dehydroxylation and complete breakdown (resulting in Kfs + Crn + H_2O) at 1 atm is approximately 560 °C. Hence, Ms dehydroxylation in our experiment, as in many other cases (e.g., Eberhart 1963; Guggenheim et al. 1987; Barlow and Manning 1999), is not an equilibrium process.

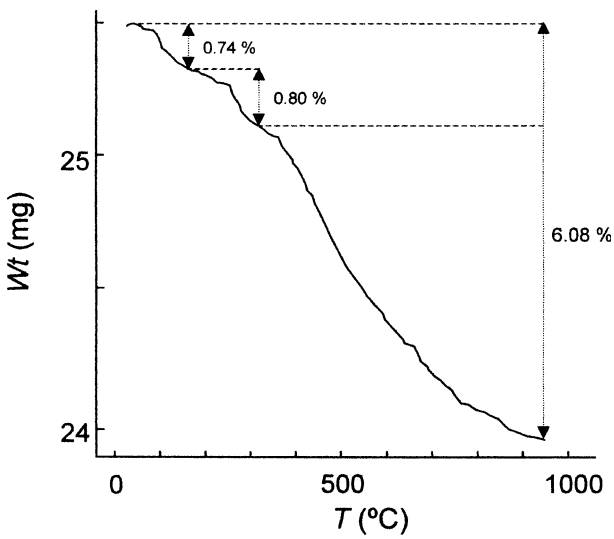

FIGURE 1. Thermogravimetric analysis of clay-rich raw material used for brick preparation. Initial weight loss corresponds to adsorbed water (0.74 wt%), second weight loss (0.80 wt%) to the initial dehydroxylation of clay minerals, and the final weight loss (4.54 wt%) to Ms (plus Ill) dehydroxylation.

Optical microscopy

Following firing at $T \geq 900$ °C, polarizing microscopy analysis revealed partially melted Ms crystals in schist fragments embedded in a low birefringent clay-rich matrix (Fig. 2a). On rare occasions the Ms crystals appear with quartz and feldspar. Detailed, higher magnification optical microscopy studies (Fig. 2b) show the presence of a melt and vestiges of non-transformed Ms. The latter displays a brownish tone and a gray interference color, probably due to partial dehydroxylation. Also observed are oriented acicular inclusions with strong relief; assumed to be Mul. These features were more common in samples fired at $T \geq 1000$ °C.

BSE and X-ray images

BSE images show important textural changes in the Ms crystals following firing. The crystals were separated along basal planes at 1000 °C when partial melting was observed (Fig. 3a). Together with structural water, K ions were lost along $(001)_{ms}$ as evidenced by a depletion in K in the adjacent basal planes (see K X-ray map in Fig. 3b). K depletion along Ms basal planes seems to be associated with the presence of Mul or a K-poor melt. The qualitative depletion in K inferred from X-ray maps is consistent with quantitative EPMA and AEM analyses (see below). Interestingly, no chemical change or reaction was detected at the Ms/Qtz interface (Fig. 3c). BSE images showed alternating bright and dark areas along partially melted Ms grains (Fig. 4a), the brighter areas corresponding to partially dehydroxylated Ms, the darker ones to a Mul-enriched melt, as revealed by Si X-ray mapping (Fig. 4b). In some areas, and in a more advanced transformation stage, bubbles that form due to H_2O release from dehydroxylating mica were observed in the brick fired at 1000 °C (Fig. 5a). These partially melted Ms crystals show slight K (Fig. 5b) and Si (Fig. 5c) depletions along the bubble edges. Ms pseudomorphs with a similar bubble structure (i.e., the so-called "cellular structure") have been described elsewhere (Tite and Maniatis 1975).

EPMA microanalysis

It should be noted that EPMA could only be used for to analyze the slightly dehydroxylated Ms grains (samples fired at 700 °C) and the higher-T Ms pseudomorphs (i.e., overall composition of the phases formed after Ms breakdown). Analyses of the melt or Mul formed after Ms breakdown could not be obtained because of their very fine-grained nature. The latter phases were therefore analyzed using AEM. Table 2 shows the composition of selected Ms grains (and pseudomorphs) fired at 700, 1000, and 1100 °C. Corresponding to the analysis (Ms2) in Table 2, a representative formula for Ms fired at 700 °C is $K_{0.844}Na_{0.117}(Al_{1.891}Fe_{0.053}Mg_{0.051}Ca_{0.002}Cr_{0.001}Ti_{0.008})(Al_{0.999}Si_{3.001})O_{10}(OH)_2$.

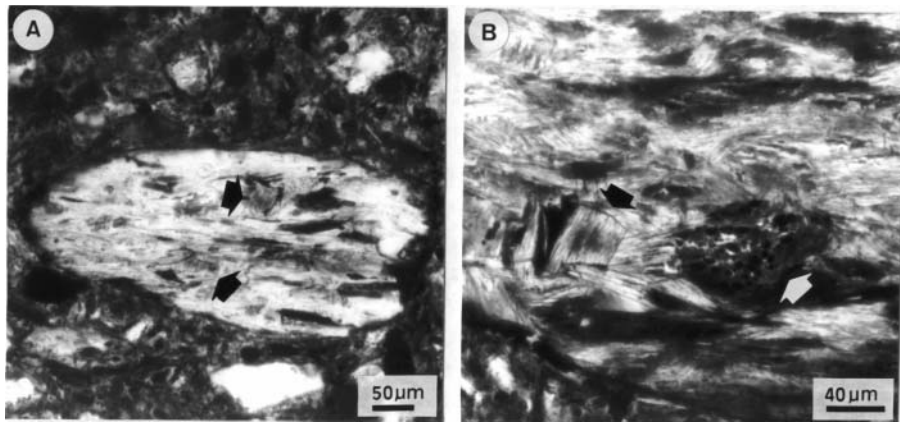

FIGURE 2. Optical microscopy images of Ms pseudomorphs in a brick sample fired at 1000 °C (crossed polars). (**A**) Partially melted schist fragment. Two large Ms crystals are observed (arrows). (**B**) Higher magnification optical image of another schist fragment with a melt pocket (white arrow) within a Ms grain. Oriented, high relief inclusions, probably Mul, can be observed within a Ms crystal (black arrow).

TABLE 2. Representative composition (in wt%) of Ms crystals fired at different *T*

	Ms1 700 °C	Ms2 700 °C	Ms3 1000 °C	Ms4 1000 °C	Ms5 1100 °C	Ms6 1100 °C	Ms7 1100 °C	Ms8 1100 °C
SiO_2	44.51	45.33	43.5	46.46	49.03	50.56	49.74	49.56
TiO_2	0.28	0.26	0.23	0.17	0.28	0.30	0.20	0.22
Al_2O_3	31.53	36.15	32.69	36.48	38.23	36.69	41.49	38.36
Cr_2O_3	0.03	0.02	0.02	0.01	0.03	0.04	0.05	0.02
Fe_2O_3	1.73	1.11	2.69	1.08	2.06	2.64	1.08	1.90
MnO	–	–	0.02	0.01	0.02	0.03	0.02	0.04
MgO	1.03	0.42	0.47	0.52	0.99	1.12	0.31	1.68
CaO	0.01	0.03	0.14	0.02	0.36	0.39	0.36	0.41
Na_2O	0.81	1.28	2.25	0.93	1.90	1.78	1.99	1.90
K_2O	8.78	8.83	8.41	10.03	5.49	5.33	4.90	5.61
Total	88.71	93.43	90.42	95.71	98.39	98.88	100.14	99.70

Note: – = not detected.

The Ms displays some paragonitic, phengitic, and illitic substitution. Analyses of low-*T* Ms consistently have totals significantly <95 wt%. This is primarily due to the fact that EPMA does not quantify water. It is also, though to a lesser extent, a result of the limited loss of K during incipient dehydroxylation. Loss of K following dehydroxylation is more evident in the high-*T* Ms pseudomorphs. In fact, the K/Si ratio decreases from ~0.27 in the 700 °C Ms to ~0.12 in the 1100 °C Ms pseudomorphs. In the latter samples the total oxide content approaches 100 wt%, a value consistent with complete dehydroxylation.

TEM images

Low-magnification TEM analysis of samples fired at 800 °C shows no clear evidence of Ms melting. However, parting of Ms crystals along basal planes was observed. Samples fired at $T \geq 900$ °C show the presence of a melt and Mul formed after Ms breakdown. Three distinctive stages in the process of Mul formation after Ms breakdown were identified, all of which can be observed within the area of a single thin foil (Fig. 6). The first stage (Stage 1 in Fig. 6) corresponds to the formation of several scattered pockets or "boxes" filled with a melt and Mul nanocrystals within the Ms host (Figs. 6a and b). These so-called boxes are generally rectangular and elongated following a specific crystallographic orientation within the Ms grains, i.e., their longest axis is parallel to the $(001)_{ms}$ basal planes. Most Mul crystals display no contact relationship with the Ms as they are surrounded by melt. However, in some cases, there does seem to be a contact (Fig. 7a). As can be seen in Fig. 7a, dehydroxylation of Ms results in the formation of defects along $(001)_{ms}$, which end in areas where the Ms structure is distorted, most likely due to incipient melting. In those areas prismatic Mul crystals are associated with more extensive volumes of melt, with one end apparently attached to the Ms and the other facing the melt in the direction in which the melting progresses. The second stage (Stage 2 in Fig. 6) is characterized by the presence of Ms pseudomorphs, which include multiple iso-oriented Mul crystals surrounded by melt (Fig. 6c). Prismatic Mul crystals in samples fired at 1000 °C are more abundant, thicker, and longer than those formed at 900 °C. The last stage of the process (Stage 3 in Fig. 6) is characterized by the presence of multiple cross-cutting Mul fibers that fully replace the Ms grains (Fig. 6d). Some of these fibers, which grow preferentially in the **c** axis direction, cross each other at an angle of 60° (or 120°) (Fig. 7b). This orientation among Mul fibers seems to be preserved from previous stages and corresponds to specific crystallographic directions within the precursor Ms grains. A similar orientation was first observed by Sundius and Byström (1953) in Mul formed after Ms breakdown at 1000–1260 °C. This orientation is also common in Mul formed after Kao (Kingery 1960). However, in our Ms pseudomorphs other fibers cross each other at a random orientation. This was also observed by Sundius and Byström (1953) and suggests further Mul crystallization in the final stages of the process, i.e., during cooling of the bricks.

High-magnification TEM analysis of both phases in Stage 2 corroborates the crystallographic correspondence between Ms

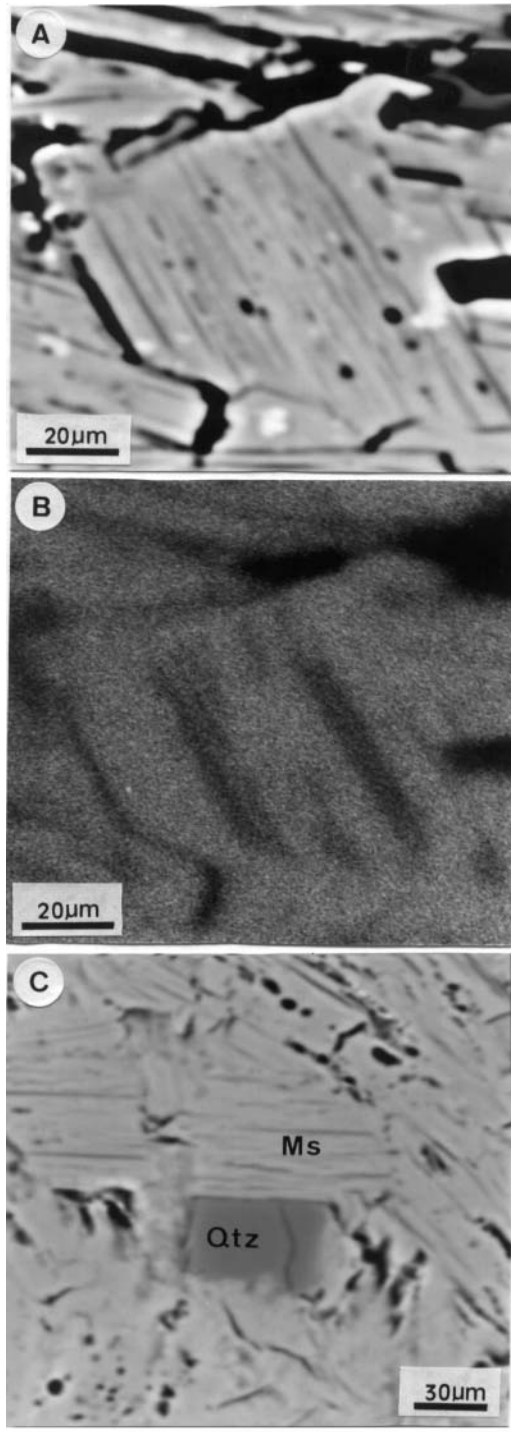

FIGURE 3. (**A**) BSE image of Ms crystals similar to those shown in optical images (sample fired at 1000 °C). The central Ms crystal is partially melted as indicated by the bubbles formed upon the release of structural water. (**B**) Potassium X-ray image of the Ms crystals in Figure 3a. The K-depleted bands may correspond to oriented Mul inclusions. (**C**) BSE image of an unreacted Ms crystal adjacent to Qtz. Note how muscovite crystals located on the top and bottom-left corner of the photograph show clear evidence of melting.

orientation and newly formed Mul fibers. All Mul crystal **c**-axes in the boxes are oriented parallel to $(001)_{ms}$ (Figs. 8a and b). The lattice fringe image in Figure 8c shows the 20 Å Ms d_{001}-spacing corresponding to a $2M_1$ polytype. It also shows the ~7.5 Å d_{010}- and d_{100}-spacings in a basal section of Mul. The **c** axis of this Mul crystal is parallel to $[010]_{ms}$ or to the symmetrically equivalent $<310>_{ms}$ zone axis, as can be inferred from the electron diffraction pattern (Fig. 8d). The **a** (and **b**) axes of all the Mul crystals within a particular box appear to be parallel (Figs. 6 and 8) and form an angle of close to 30° (or 60°) with $(001)_{ms}$. In particular, the SAED image (Fig. 8d) evidences that $\mathbf{c}^*_{ms}$ is sub-parallel to $<120>_{mul}$ [i.e., $(001)_{ms}$ is quasi-parallel to $(120)_{mul}$ or $(210)_{mul}$]. This latter orientation is also observed in various boxes within many Ms crystals (Figs. 6c and 8a).

In a more advanced stage of Mul development many crystals coalesce into larger mosaic crystals and their **a** (and **b**) axes display a disorientation of only several degrees due to rotation around the **c** axis. The resulting electron diffraction image shows the $[001]_{mul}$ zone axis patterns from different coherent scattering domains (i.e., crystallites) rotated relative to one another around the **c** axis (Fig. 9a). This mismatch is only observable in high-order electron diffraction reflections and is hard to see when observing HRTEM images of Mul crystals cut perpendicular to the **c** axis (Fig. 9b). It seems that many Mul nuclei started to grow competitively out of the same substrate, as will be discussed later.

Stage 3 is characterized by well-developed elongated Mul fibers that grow along **c** in an oriented (i.e., almost parallel) or randomly oriented (more common) manner. Moiré fringes can be observed (Fig. 10a) because of the superposition of Mul crystals with contrasting orientations (e.g., the observed 60° in Fig. 6d). A section perpendicular to the longest fiber axis (Fig. 10b) reveals that the number of fibers (aggregates surrounded by melt) at this later stage is very high (~250 crystals/µm^2), thus suggesting a complete transformation of Ms into Mul + melt. The amount of melt appears to be drastically lower when compared to previous stages. This points to further Mul crystallization and growth during cooling of the melt, which is consistent with the random orientation of some Mul crystals in Figures 6d and 8a (lower right corner).

AEM analysis

AEM results for Ms crystals and Ms high-*T* breakdown products are presented in Table 3. Corresponding to analysis 1, a representative formula for Ms fired at 1000 °C is

TABLE 3. Representative AEM composition (expressed as wt% oxides) of Ms, Mul, and melt (sample fired at 1000 °C)

	Ms		Mul		Melt		
	Ms(1)	Ms(2)	Mul(1)	Mul(2)	Melt(1)	Melt(2)	Melt(3)
SiO_2	49.41	52.28	31.23	30.45	60.16	67.86	59.50
TiO_2	1.10	0.22	–	0.77	–	–	1.07
Al_2O_3	35.14	33.25	63.93	63.21	24.11	22.86	26.68
Fe_2O_3	5.10	2.37	4.61	3.92	3.32	1.58	2.45
MgO	0.99	1.24	0.95	1.64	1.94	0.73	–
NaO	0.74	1.31	–	–	3.21	1.81	3.84
K_2O	7.52	9.33	–	–	7.26	5.15	6.44
Total	100	100	100	100	100	100	100

Note: – = not detected.

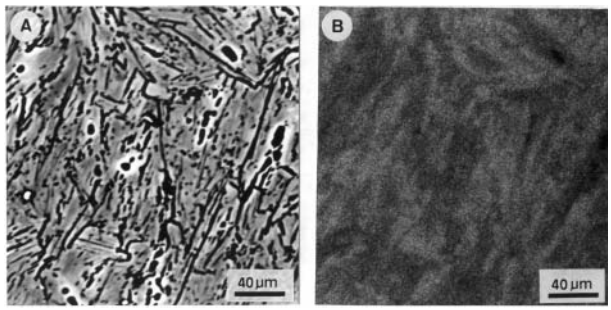

FIGURE 4. (**A**) BSE image of a partially melted Ms aggregate (sample fired at 1000 °C). (**B**) Potassium X-ray image of the same area. Lighter areas correspond to relatively well-preserved Ms crystals and darker ones to a melt enriched in Mul. No Qtz has been observed in this area in the Si X-ray image (not shown).

$K_{0.602}Na_{0.090}(Al_{1.777}Ti_{0.052}Fe_{0.240}Mg_{0.093})(Al_{0.818}Si_{3.102})O_{10}(OH)_2$.

The Ms composition is consistent with the EPMA results (Table 2) and thus corroborates the accuracy of the AEM analyses. As for the Ms samples fired at 700–1100 °C (EPMA analyses), these Ms also show a significant amount of paragonitic, phengitic, and illitic substitution, and the K content is relatively low due to K loss during Ms dehydroxylation.

In terms of the formula $^{[6]}Al_2{}^{[4]}(Al_{2+2x}Si_{2-2x})O_{10-x}$, which takes into account the presence of O atom vacancies (Cameron 1977), one formula representative of Mul composition is $^{[6]}(Al_{1.686}Ti_{0.031}Fe_{0.159}Mg_{0.134})\ ^{[4]}(Al_{2.360}Si_{1.657})O_{9.82}$ (Mul analysis 2). This composition yields an x value of 0.18, which is slightly lower than that obtained by XRD (x = 0.25). This discrepancy could be accounted for by considering that some $^{[6]}$Al is replaced by Fe^{3+}, Ti, or Mg, elements that were not considered by Cameron (1977) and that induce slight changes in the crystallographic parameters (Chaudhuri and Patra 2000). The presence of Fe^{3+}, Ti, and Mg in Mul has been reported extensively (Agrell and Smith 1960; Cameron 1977; Rubie and Brearley 1987; Brearley and Rubie 1990; Chaudhuri and Patra 2000). In particular, Fe^{3+} is preferentially incorporated into 3:2-Mul at the octahedral positions, when compared to 2:1-Mul (Schneider and Pleger 1993). The Mul we studied is close to a 3:2-Mul and highly similar to that reported by Rubie and Brearley (1987), who also applied AEM to the study of Mul formed after Ms breakdown. Raterron et al. (1999 and 2000) found Mul formed following Sil mullitization with x values of ~0.17. The authors suggested that these non-stoichiometric 3:2-Mul samples could be an intermediate phase (i.e., solid solution) between Sil and Mul.

The melt formed in the first stage of Mul growth is enriched in Si and depleted in Al when compared to the former mica. This may be due to the fact that Al is preferentially included in the newly formed Mul. Although alkalis (Na and K) are present in the melt, their overall concentrations are lower when compared to those of dehydroxylated Ms.

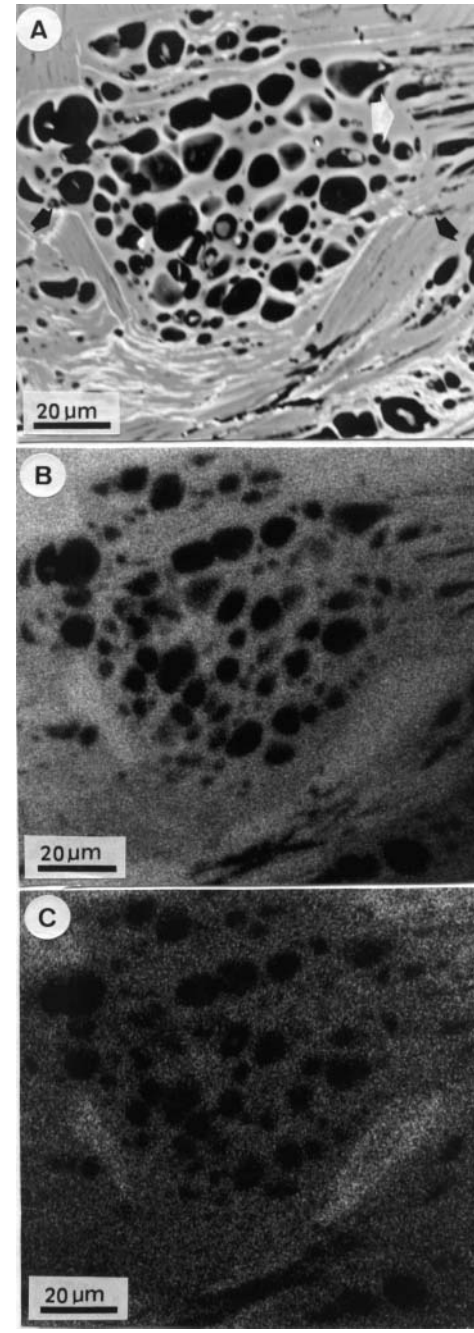

FIGURE 5. (**A**) BSE image of a melt after Ms (sample fired at 1000 °C). Numerous rounded bubbles appear in areas affected by extensive melting (center of the image). Elongated pores (white arrow) indicate the morphology of former Ms crystals. Some Ms crystals adjacent to the melt appear to be relatively well preserved (black arrows). (**B**) Potassium X-ray image and (**C**) Si X-ray image corresponding to the area shown in (**A**). Lighter zones (i.e., higher K or Si concentration) in both images correspond to well-preserved Ms crystals.

DISCUSSION

Ms dehydroxylation

High-*T*/low-*P* Ms breakdown followed by Mul growth begins with the mica dehydroxylation process. The loss of Ms

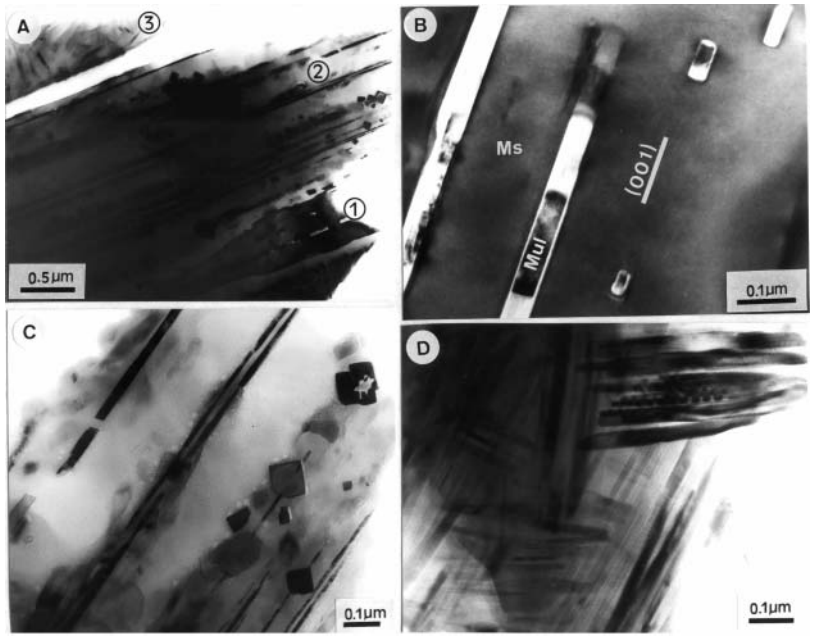

FIGURE 6. (**A**) Low-magnification TEM image showing the three stages in the process of Mul development after Ms breakdown. At Stage 1, box-like melt pockets develop within Ms and Mul crystals start to grow within them. In Stage 2, Ms pseudomorphs are replaced by oriented Mul fibers and melt, whereas in Stage 3 massive Mul replaces Ms (observed here in a Ms pseudomorph adjacent to the one showing the two previous stages). (**B**) Box-like inclusions of Mul + melt following basal planes of the Ms host during Stage 1. Mul appears in the center of these boxes surrounded by very thin rims of melt. (**C**) Oriented Mul + melt corresponding to Stage 2. Basal and longitudinal sections of Mul crystals define two sets of orientations in the melt. (**D**) Detail of massive Mul aggregate + melt in Stage 3. Some sets of oriented aggregates of Mul fibers preserve the 60° orientation in Stage 2, however other fibers show random orientations.

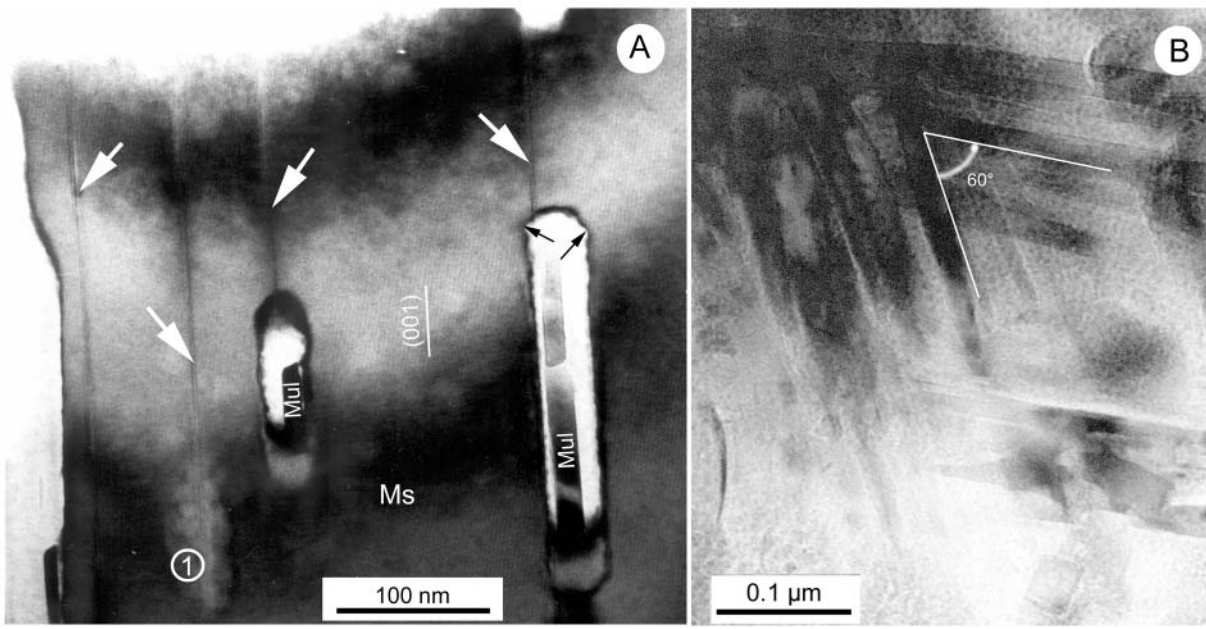

FIGURE 7. TEM image of Ms fired at 900 °C showing: (**A**) Mul growth during Stage 1. Flaws (white arrows) develop along Ms basal planes. One of them is connected to an area of initial Ms melting (point 1), while two others are connected to already developed melt pockets with Mul prismatic crystals. Mul crystals appear to be anchored on the Ms. Note that melting progresses toward the Ms forming semicircular concave structures (black arrows). (**B**) Detail of Mul fibers cross-cutting at 60° in a Ms pseudomorph oriented with its **c** axis normal to the image plane.

OH groups is a complex, step-wise process that takes place when $T > 550$ °C, as can be inferred by thermal analysis (Kodama and Brydon 1968; Guggenheim et al. 1987; Barlow and Manning 1999) and dynamic high-*T* X-ray powder diffraction (Mazzucato et al. 1999). In Ms crystals, the dehydroxylation does not seem to progress homogeneously. In fact, it probably first takes place when a defect triggers OH^- release from neighboring Al-octahedra. OH groups in the octahedral sheets are lost according to the following reaction: $2(OH) \rightarrow H_2O + O$, in which the residual O atoms move to the *z*-coordinate position of the Al cation (Guggenheim et al. 1987). On the other hand, Aines and Rossman (1985) proposed that H migration toward a neighboring OH group would result in H_2O generation upon Ms dehydroxylation. The resulting H_2O molecule moves out of the structure, first monodimensionally along distorted sixfold coordinated Al rings (Mazzucato et al. 1999) and later, bidimensionally along Ms basal planes (Gaines and Vedder 1964; Sanchez-Navas 1999); the diffusion of water out of the structure is the

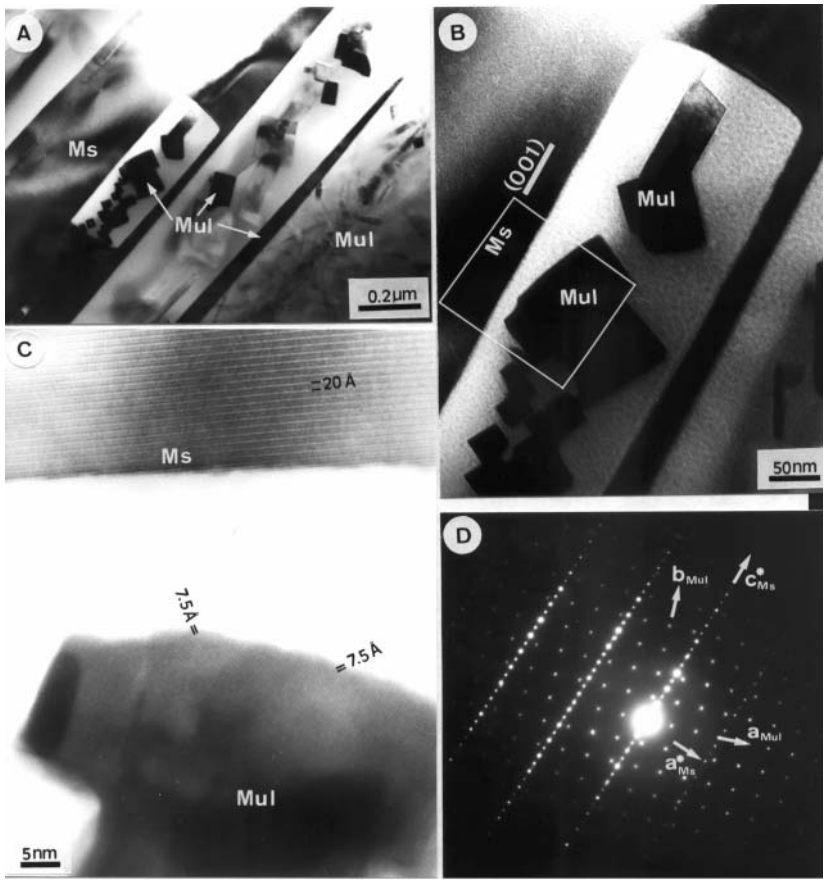

FIGURE 8. (**A**) Low-magnification TEM image of the three stages of the Ms to Mul transformation. (**B**) Detail of a box-like inclusion in (**A**). Most Mul fiber **c**-axes in this inclusion are perpendicular to the image plane and parallel to Ms basal planes. (**C**) Enlarged image of the region outlined in (**B**) showing lattice fringes with a d_{001}-spacing of 20 Å that correspond to a two-layer polytype of Ms, and d_{100} and d_{010} spacings of approximately 7.5 Å in a basal section of a Mul crystal. (**D**) SAED pattern at the Ms-Mul boundary shown in image (**c**). Mul orientation corresponds to that of the basal section as observed in the crystal of image (**C**); the **c*** and **a*** crystallographic axes of the adjacent Ms are also visualized, so that the Mul **c**-axis coincides with $[010]_{ms}$ or with the equivalent $<310>_{ms}$.

rate-limiting process. Alkalis (i.e., K and Na) are lost together with water (Grapes 1986; Sanchez-Navas 1999) and most probably accumulate in the porous clayey matrix of the brick, an observation that is consistent with our potassium X-ray maps and AEM and EPMA results.

Ms undergoes significant textural changes during dehydroxylation. First, Ms exfoliates along basal planes due to K plus H_2O loss (Cultrone et al. 2001). When melting overlaps dehydroxylation, bubbles with trapped water vapor develop; initially they are elongated, whereas later on they become almost spherical. Bubble formation leads to the so-called "cellular structure" observed in Figure 5 and first described by Tite and Maniatis (1975). A cellular structure only develops under rapid heating conditions (i.e., during ceramic firing).

Structurally, the dehydroxylation process results in a significant transformation of the Ms octahedral sheet, where Al changes from a sixfold to a fivefold coordination, as shown in Figure 11a (Udagawa et al. 1974; Guggenheim et al. 1987; Abbott 1994; Mazzucato et al. 1999). High-temperature Ms structural analyses have shown that dehydroxylation is almost complete at ~850 °C (in a time scale of a few hours); OH groups are lost at lower *T* when neighboring Al are in sixfold coordi-

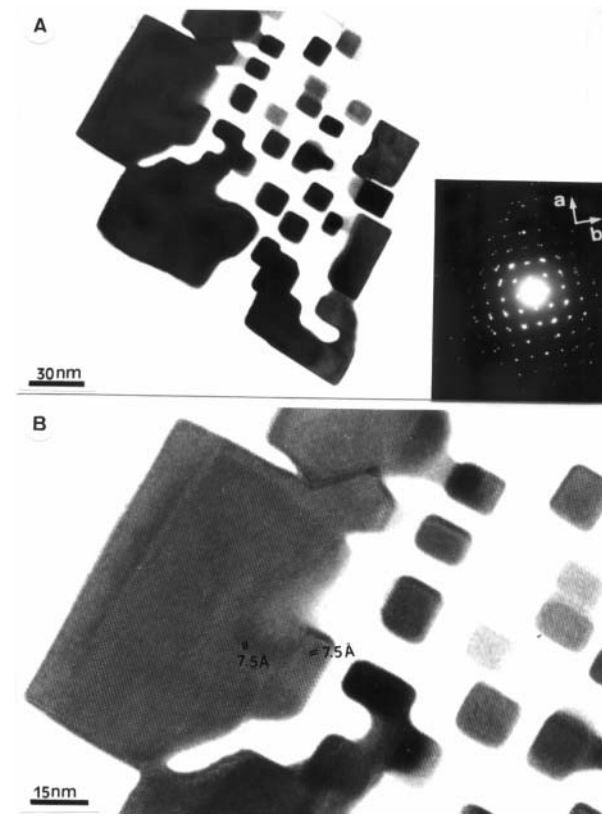

FIGURE 9. (**A**) Skeletal Mul crystals observed along their **c** axes. The electron diffraction pattern (inset) shows rotation of the individual fibers around the **c** axis. (**B**) HRTEM image of this Mul basal section.

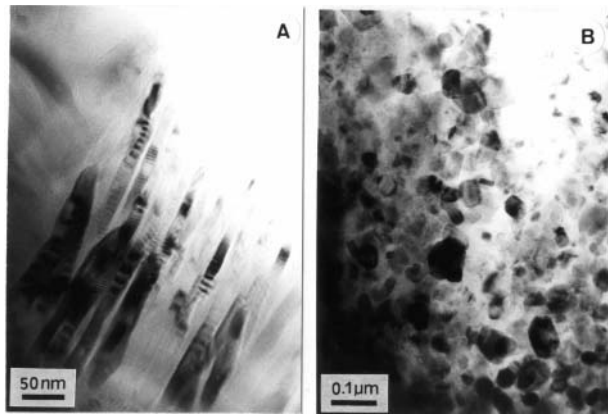

FIGURE 10. (**A**) Oriented aggregate of Mul fibers observed along a longitudinal section. Abundant moiré fringes are a result of the superposition of these fibers over other crystals not visible in the image. (**B**) Mul aggregate similar to that shown in (**A**), but with Mul **c** axes oriented almost perpendicular to the image plane.

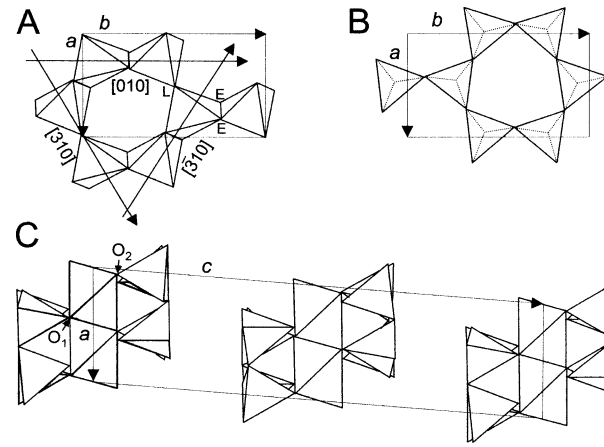

FIGURE 11. (**A**) Dehydroxylated Ms "octahedral" (i.e., pentahedral) sheet projected on (001) (after Udagawa et al. 1974; Guggenheim et al. 1987). Al-pentahedral crankshaft-like chains running parallel to $[310]_{ms}$, $[\bar{3}10]_{ms}$ and $[010]_{ms}$ can be observed. (**B**) Dehydroxylated Ms tetrahedral sheet projected on (001) (after Udagawa et al. 1974) showing tetrahedral crankshaft-like chains running parallel to $[310]_{ms}$ $[3\bar{1}0]_{ms}$ and $[010]_{ms}$. (**C**) Ms T-O-T structure projected on (010). See text for details.

nation, and at higher *T* in partially dehydroxylated Ms with neighboring Al in fivefold coordination (Guggenheim et al. 1987). The latter observations explain the step-wise nature of the dehydroxylation process evidenced by TGA. The dehydroxylated Ms has strongly bonded Al-pentahedra crankshaft-like chains along $<310>_{ms}$ and $[010]_{ms}$ with a high density of apical bonding (Fig. 11a). Hence, these equivalent strong-bonding directions (at an angle of 60°) are the main periodic bond chains (PBC) (Hartman and Perdock 1955) of dehydroxylated Ms octahedral sheets. The tetrahedral sheet is also deformed as shown in Figure 11b (structural data for dehydroxylated muscovite after Udagawa et al. 1974).

Ms partial melting and epitaxial nucleation of Mul

Dehydroxylated Ms can be considered an unstable activated phase that may easily undergo local melting as *T* rises. Once the melt is formed (first melting is observed at 900 °C), Mul nucleation and growth occurs in specific areas when supersaturation (i.e., undercooling) is sufficient. All Mul crystals within the "boxes" in Stages 1 and 2 of Mul growth are oriented in very specific directions with respect to Ms. Their **c** axes are parallel to $(001)_{ms}$; in particular, $[001]_{mul}$ is parallel to $[010]_{ms}$ or to the equivalent $<310>_{ms}$. Based on previous work by Bradley and Grim (1951) on the high-*T* pyrophyllite to Mul transformation, Eberhart (1963) first noted that Al "octahedral" chains in anhydrous Ms were similarly oriented along $[001]_{mul}$. In addition, Mul $(120)_{mul}$ [or the equivalent $(210)_{mul}$] planes within the boxes in Stage 2 are subparallel to $(001)_{ms}$ (HRTEM and SAED results).This latter orientation was also first observed by Eberhart (1963) by means of XRD analyses of Mul formed after Ms. These findings suggest that a structural relationship of some kind between Ms and Mul controls Mul formation. Our data point to Mul epitaxial nucleation and growth (from a supersaturated melt) on partially melted dehydroxylated Ms. This would be the most plausible explanation for all the systematic structural relationships observed, as will be discussed below.

Partial melting of dehydroxylated Ms results in the melt pockets and should have taken place through the breaking of bonds between edge-sharing Al-pentahedra, since the mica "octahedral" sheet is less stable than the tetrahedral sheet (Barlow and Manning 1999). According to Pauling's ionic bond theory, the bonding stability of coordination polyhedra increases from edge- to corner-sharing due to the closer proximity between cations in the former. Therefore, bond-breaking will most probably occur along weakly bonded pairs of edge-shared O atoms (E O atoms in Fig. 11a). Once the Al-pentahedra face the melt, they could rapidly transform into the more stable octahedra by incorporating an O atom. The octahedra, to which Al- and Si-tetrahedra (i.e., portions of the Ms T-O-T structure) could be attached, form chains along the $<310>_{ms}$ or $[010]_{ms}$ directions (see Fig. 11c). The two O atoms of the outermost edge of the octahedra, which are parallel to $(110)_{ms}$ or $(010)_{ms}$ (i.e., atoms O_1 and O_2 in Fig. 11c), will face the peraluminous melt. This orientation of the O atoms is only achieved in planes perpendicular to $<310>_{ms}$ or $[010]_{ms}$. These Ms portions (i.e., octahedra edges) located at the mica-melt interface will act as a template for Mul heterogeneous nucleation and growth. In this manner the original orientation of Ms edge-sharing Al-octahedral chains is preserved. The octahedral chains now become the backbones of the Mul crystals. In fact, the 3:2-Mul (orthorhombic, space group *Pbam*) backbones are edge-sharing AlO_6 octahedra chains parallel to the **c** axis (Fig. 12a and b). At 1/2 *c*-value (~2.9Å) in each Mul cell, the octahedral chains are cross-linked to SiO_4 and AlO_4 tetrahedra, forming double-chains parallel to $[001]_{mul}$ (Saalfeld and Guse 1981; Angel and Prewitt 1986; Angel et al. 1991; Balzar and Ledbetter 1993; Rehak et al. 1998). The edge-sharing Al-octahedra along the $[010]_{ms}$ and $<310>_{ms}$ directions therefore perfectly match those running along $[001]_{mul}$. This explains one of the systematic orientations

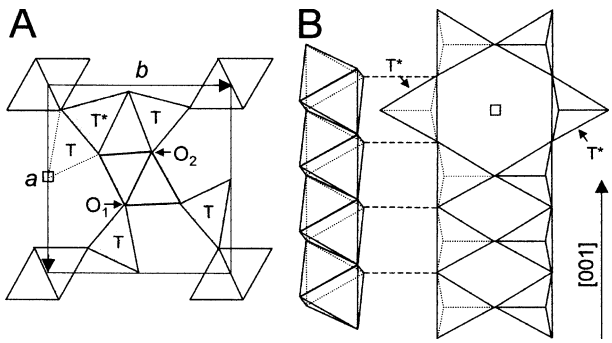

FIGURE 12. (**A**) Mul unit cell projected on (001) showing T (Si, Al) and T* (Al) tetrahedral positions and O atom vacancy □ (Rahman and Weichert 1990; Balzar and Ledbetter 1993). Positions of the two O atoms (O_1 and O_2) at the upper edge of the central octahedron are indicated. (**B**) 3/2-Mul structure with edge-sharing $^{[6]}$Al chains along $[001]_{mul}$; the tetrahedral "Einer-Doppelkette" point "inward" (i.e., T positions) and the tetrahedral "Zweier-Doppelkette" "outward" (i.e., T* tetrahedral positions); □ indicates a vacancy (i.e., O atom deficit of 1:8) (Pannhorst and Schneider 1978; Saalfeld and Guse 1981).

observed: i.e., $[010]_{ms}$ and $<310>_{ms}$ are || to $[001]_{mul}$. The subparallel orientation between $(120)_{mul}$ [or $(210)_{mul}$] and $(001)_{ms}$ may be due to the fact that the two upper-edge O atoms in each Al-octahedron in the $(001)_{mul}$ plane are parallel to either $[120]_{mul}$ or $[210]_{mul}$ (i.e., atoms O_1 and O_2 in Fig. 12a). This orientation matches that of the octahedra in the Ms T-O-T structure in those sections parallel to $(110)_{ms}$ and $(010)_{ms}$ (i.e., O atoms O_1 and O_2 in Fig. 11c).

Though no completely clear contact relationship could be seen between Ms and Mul in Stage 1 of Mul growth, this does not imply that no contact exists three-dimensionally or ever existed in the very early stages of the process (i.e., heterogeneous nucleation of Mul). The notorious excess of melt in the Ms → Mul transformation (TEM results), which may be located at the Ms-Mul boundary, should preclude the maintenance of a long-term interface between both phases.

This epitaxial model for Mul formation after Ms is consistent with the parallel orientation of Mul crystals in the "boxes" and with the 60° orientation among different sets of Mul crystals within a Ms host: e.g., the 60° orientation between some sets of Mul crystal **c**-axes that corresponds to the former $<310>_{ms} \wedge [010]_{ms}$. If random nucleation had taken place in a pool of melt within the mica crystal, a systematic orientation of all the nucleating crystals would be unlikely. A topotactic replacement could also explain the systematic orientation. However, a topotactic replacement seems less plausible for two reasons: first, because the large structural differences between both phases requires a very complex rearrangement to adapt the structure of Ms to that of Mul, and this process would be less favorable energetically; and second, because the development of a large volume of melt precludes the long term preservation of a contact boundary between both phases.

Mul coarsening and further crystallization during cooling

In Stage 2, the melt from different "boxes" coalesces into a large pool of peraluminous melt that contains many needle-shaped Mul crystals elongated along their **c** axes. Mul can grow very quickly along $[001]_{mul}$, where AlO_6 octahedral chains exist. These are the most stable structural units in the aluminum silicates (Schneider et al. 1994; Hülsmans et al. 2000) and they act as the main Mul PBC. The final Mul microstructure is the result of many grains coalescing, thus reducing both surface area and surface energy. These large Mul grains show a mosaic structure in Stage 3. In fact, the coarsening process indicates a mismatch of several degrees in the $[100]_{mul}$ (and $[010]_{mul}$) directions among previously independent Mul crystals. The slight misorientation among different Mul domains is probably inherited from the former mica, which may display slight changes in the orientation of the octahedra of different domains. Apparently, many Mul nuclei started to grow competitively out of the same substratum. The growth (along the **a** and **b** axes) of those crystals located in the outer parts was faster than in those located in the center, which accounts for their skeletal shape. This is due to the higher silica and alumina concentrations in the melt surrounding the former crystals. In fact, the Mul crystals in the center are surrounded by many other crystals and therefore face an alumina- and silica-poor melt. In addition, the overall shape of the Mul mosaic crystals (such as that in Fig. 9) is typical of a crystal grown in a highly supersaturated media (Mullin 1992).

Once the oven was turned off, significant undercooling of the melt induced nucleation and growth of Mul crystals with a random orientation, as observed in the TEM images. Classic crystallization theory predicts that high supersaturation (or undercooling) will promote a high nucleation rate (Tiller 1991; Putnis 1992; Mullin 1992), resulting in many crystals that grow rapidly along their main PBCs (Sunagawa 1981). This is consistent with the large number of randomly oriented Mul crystals growing along the $[001]_{mul}$ direction in the fully transformed Ms pseudomorphs. Due to the high nucleation density and the shorter growth time (until full solidification of the melt), these latter crystals are smaller and thinner than those formed epitaxially in the early stages of the process, as can be observed in the TEM images.

Ms → Mul reaction pathways

Following Ms dehydroxylation, a melt forms with an almost Ms-like composition, however, it is probably H_2O-unsaturated and K-depleted. This reaction is similar to that reported by Brearley and Rubie (1990) for disequilibrium Ms breakdown in H_2O-undersaturated conditions. The melting, first observed in samples fired at 900 °C, is defined by

$$\text{Ms} \rightarrow \text{melt} + H_2O \quad (1)$$

Mul nucleation occurs almost contiguously at $T \geq 900$ °C, once enough melt exists and sufficient supersaturation is reached.

Existing data on high-*T* and low-*P* Ms breakdown and Mul formation point to the following overall reaction (Sundius and Byström 1953):

$$\text{Ms} \rightarrow \text{Crn/Mul} + \text{melt} + H_2O \quad (2)$$

Grapes (1986) indicates that Ms with several per cent Fe

breaks down to form Crn and/or γ-Al_2O_3 with little Mul, whereas Fe-poor Ms (i.e., our Ms) develops little Crn and abundant Mul. Eberhart (1963) also found that only Mul (as opposed to Crn) formed after high-*T* breakdown of Fe- (and Mg-) poor Ms.

Considering the previous reaction 2 pathway for Ms decomposition, and the actual composition of the melt formed upon Ms breakdown in our system (e.g., melt analysis 3 in Table 3), the overall theoretical mass-balanced reaction for the K_2O-Al_2O_3-SiO_2-H_2O system can be expressed as

$$1Ms = 0.375Mul + 0.75\ Melt(3) + 0.382K_2O + 0.125H_2O \quad (3)$$

According to the previous reaction 3 and the AEM results (Table 3), the following balanced reaction for the transformation of Ms into Mul plus a melt can be obtained by regression analysis (estimated standard error: 0.02):

$$1Ms(1) = 0.257\ Mul(1) + 0.667Melt(3) + 0.244K_2O + 0.010Na_2O + 0.125H_2O \quad (4)$$

Reaction 4, which applies to the early stage of Mul growth, demonstrates that Mul formation after Ms breakdown leads to the generation of a residual peraluminous melt. This melt formed in reaction 1 leads to the nucleation of the first Mul crystals. The residual peraluminous melt in reaction 4 has an Al/Si ratio of 1/2, which is not consistent with Kfs (i.e., Al/Si ratio of 1/3), and that could allow further Mul growth during cooling (i.e., during Stage 3). Reaction 4 also shows that alkalis are partially lost during the process, probably due to their high mobility along dehydroxylated Ms basal planes (Sanchez-Navas 1999). Water is lost in the same way as dehydroxylation progresses.

On the basis of the K_2O-Al_2O_3-SiO_2 system (Schairer and Bowen 1947), Grapes (1986) states that anhydrous Ms should break down into the following assemblages as *T* increases: Leu + Kfs + Mul, Leu + Mul + melt, and Leu + Crn + melt. Leu is however only rarely found as a by-product after high-*T* Ms breakdown and the presence of a melt instead of Kfs underscores the fact that Ms-out reactions 2, 3, and 4 are metastable, as described by Grapes (1986) for the melting of pelitic xenoliths. Sundius and Byström (1953) stated that the Schairer and Bowen (1947) phase diagram was made on glass formed directly from the constituent oxides, whereas Ms is a crystal with a definitive atomic structure and thus time is necessary to reach equilibrium. In fact, earlier works by Evans (1965) and Velde (1966) demonstrated that the end-member Ms equilibrium breakdown reaction is Ms $\rightarrow$ Kfs + Crn + H_2O and takes place at a *T* of ~560 °C and a *P* of 1 atm. These data support the metastable nature of reaction 4. The significant overstepping in reaction 4 is consistent with the rapid heating and short duration of our experiment. It should be noted that the equilibrium reaction occurred in Velde's experiment after 21 days at the above-mentioned *P* and *T* conditions. This suggests that kinetic constraints may have precluded the formation of Kfs. As previously indicated, Crn does not develop due to the low Fe content of the Ms, since Fe plays a significant role in stabilizing the Crn structure (Sundius and Byström 1953).

These results suggest that kinetic constraints could account for the formation of Mul plus a melt after Ms breakdown. Rubie and Brearley (1987) argued that the formation of Mul (or Crn) plus a metastable melt after Ms breakdown is kinetically favored by a reduction in the entropy of activation, which greatly influences the nucleation rate. Metastable phase nucleation could therefore be favored and would be much faster than the nucleation of stable phases (Putnis 1992). It should be added that in the present case significant energy reduction is also induced by the epitaxial nature of Mul growth on the remaining Ms substratum.

Melting of a mixture of oxides with a dehydroxylated Ms-like composition occurs at the ternary eutectic Tri-Mul-Kfs at a temperature of 985 °C (Muan and Osborn 1965). However, the fluxing role of water could induce a reduction of the melting *T* (Rubie 1986), since water is continuously released during Ms dehydroxylation over the entire range of experimental *T* (i.e., dehydroxylation was not completed at *T* ~950 °C according to TGA).

The 900 °C temperature reported for the first occurrence of both melt and Mul is somewhat higher than those reported by Brearley and Rubie (1990) for the disequilibrium breakdown of Ms at 1 Kbar (i.e., 680 and 757 °C for melt and Mul occurrence, respectively). According to these authors, low pressure stable melting of end-member Ms should occur at ~970 °C. However, in the presence of water (Rubie 1986; Rubie and Brearley 1987) and in a multicomponent system (e.g., Ms with some Na, Mg, and Fe), stable melting should occur at a slightly lower but unknown temperature. In our case, this uncertainty precludes a conclusive statement regarding the stable or metastable nature of the melt formed upon Ms breakdown. Nonetheless, it would seem likely that metastable melt formation does occur, particularly if one considers that the very first melting should have taken place at a (unknown) *T* between 800 and 900 °C.

In conclusion, thermal energy is minimized by epitaxial nucleation and growth of Mul in a melt after Ms breakdown. In addition, H_2O released upon Ms dehydroxylation plays a fluxing role. On the other hand, the multicomponent nature of the melt formed after Ms breakdown induces nucleation of Mul at a lower *T* than that predicted by the equilibrium phase diagram. The presence of K, Na, Mg, and Fe in the melt leads to a significant lowering of Mul crystallization *T* (see systems Al_2O_3-SiO_2-K_2O and Al_2O_3-SiO_2-Na_2O in Schairer and Bowen 1947, and systems Al_2O_3-SiO_2-FeO and Al_2O_3-SiO_2-MgO in Muan 1957, Osborn and Muan 1960, and Muan and Osborn 1965). The previous three factors could explain why Mul appears at *T* ~ 900 °C. This is almost 100 °C below the SiO_2-Al_2O_3-K_2O ternary system eutectic (after a melt with an end-member Ms composition).

Finally, an analysis of published results for Mul formation, both in nature and in the laboratory, allows us to propose that this epitaxial model for Mul formation be extended to other dioctahedral 2:1 and 1:1 phyllosilicates, such as pyrophyllite (Bradley and Grim 1951; Heller 1962) and kaolinite (Kingery 1960), respectively.

ACKNOWLEDGMENTS

This work was supported by grants MAT 2000-1457 and BTE 2000-0582 from the Spanish government (DGI) and the Junta de Andalucia Research Group NMR 092. We thank the CIC of the UGR for technical assistance during TEM,

EPMA, and SEM analyses. The manuscript has benefited from suggestions by F. Camara, F. Nieto, and K. Elert. We are grateful to A.J. Brearley, W. Mader, and an anonymous referee for their in-depth reviews and helpful comments, and to M. Bettini for thorough English editing.

REFERENCES CITED

Abbott, R.N. (1994) Energy calculations bearing on the dehydroxylation of muscovite. Canadian Mineralogist, 32, 87–92.

Agrell, S.O. and Smith, J.V. (1960) Cell dimension, solid solutions, polymorphism and identification of mullite and sillimanite. Journal of the American Ceramic Society, 43, 69–76.

Aksay, I.A., Dabbs, D.M., and Sarikaya, M. (1991) Mullite for structural, electronic and optical applications. Journal of the American Ceramic Society, 74, 2343–2358.

Aines, R.D. and Rossman, G.R. (1985) The high temperature behavior of trace hydrous components in silicate minerals. American Mineralogist, 70, 1169–1179.

Angel, R.J. and Prewitt, C.T. (1986) Crystal structure of mullite: a re-examination of the average structure. American Mineralogist, 71, 1476–1482.

Angel, R.J., McMullan, R.K., and Prewitt, C.T. (1991) Substructure and superstructure of mullite by neutron diffraction. American Mineralogist, 76, 332–342.

Balzar, D. and Ledbetter, H. (1993) Crystal structure and compressibility of 3:2 mullite. American Mineralogist, 78, 1192–1196.

Barber, D.J. (1970) Thin foils of non metals made for electron microscopy by sputter etching. Journal of Material Science, 5, 1–8.

Barlow, S.G. and Manning, D.A.C. (1999) Influence of time and temperature on reactions and transformations of muscovite mica. British Ceramic Transactions, 98, 3, 122–126.

Baronnet, A. (1997) Silicate microstructures at sub-atomic scale. Geomaterials, 324, 157–172.

Bradley, W.F. and Grim, R.E. (1951) High temperature thermal effects of clay and related materials. American Mineralogist, 36, 182.

Brearley, A.J. (1986) An electron optical study of muscovite breakdown in pelitic xenoliths during pyrometamorphism. Mineralogical Magazine, 357, 385–397.

Brearley, A.J. and Rubie, D.C. (1990) Effects of H_2O on the disequilibrium breakdown of muscovite + quartz. Journal of Petrology, 31, 925–956.

Brindley, A.J. and Nakahira, M. (1959) The kaolinite-mullite reaction series: II, meta kaolin. Journal of the American Ceramic Society, 42, 314–318.

Cameron, W.E. (1977) Mullite: substituted alumina. American Mineralogist, 62, 747–755.

Champness, P.E., Cliff, G., and Lorimer, G.W. (1981) Quantitative analytical electron microscopy. Bulletin of Mineralogy, 104, 236–240.

Chaudhuri, S.P. and Patra, S.K. (2000) Electron-paramagnetic-resonance and Mössbauer-spectroscopy of transition-metal ion doped mullite. Journal of Material Science, 35, 4735–4741.

Clark, B.H. and Peacor, D.R. (1992) Pyrometamorphism and partial melting of shales during combustion metamorphism: mineralogical, textural and chemical effects. Contribution to Mineralogy and Petrology, 112, 558–568.

Cliff, G. and Lorimer, G.W. (1975) The quantitative analysis of thin specimens. Journal of Microscopy, 103, 203–207.

Cultrone, G., Rodriguez-Navarro, C., Sebastian, E., Cazalla, O., and de la Torre, M.J. (2001) Carbonate and silicate phase reactions during ceramic firing. European Journal of Mineralogy, 13, 621–634.

Deer, W.A., Howie, R.A., and Zussman, J. (1982) Rock-forming minerals (2nd edition). Vol. 1A, Orthosilicates. Longman, London.

Eberhart, J.P. (1963) Etude des transformations du mica muscovite par chauffage entre 700 et 1200 °C. Bulletin Société Française Minéralogie Cristallographie, 86, 213–251.

Evans, B.W. (1965) Application of a reaction-rate method to the breakdown equilibria of muscovite and muscovite plus quartz. American Journal of Science, 263, 647–662.

Gaines, G.L. and Vedder, W. (1964) Dehydroxylation of muscovite. Nature, 201, 495.

Grapes, R.H. (1986) Melting and thermal reconstitution of pelitic xenoliths, Wehr Volcano, East Eiffel, Germany. Journal of Petrology, 27, 243–396.

Guggenheim, S., Chang, Y.H., and van Groos, A.F.K. (1987) Muscovite dehydroxylation: High-temperature studies. American Mineralogist, 72, 537–550.

Hartman, P. and Perdock, W.C. (1955) On the relation between structure and morphology of crystals. Acta Crystallographica, 8, 49–52.

Heller, L. (1962) The thermal transformation of pyrophyllite to mullite. American Mineralogist, 47, 156–157.

Hülsmans, A., Schmücker, M., Mader, W., and Schneider, H. (2000) The transformation of andalusite to mullite and silica: Part 1. Transformation mechanism in $[001]_A$ direction. American Mineralogist, 85, 980–986.

Kingery, W.D. (1960) Introduction to ceramics. Wiley, New York.

Kodama, H. and Brydon, J.E. (1968) Dehydroxylation of microcrystalline muscovite. Transactions of the Faraday Society, 63, 3112–3119.

Kretz, R. (1983) Symbols for rock-forming minerals. American Mineralogist, 68, 277–279.

Martin Ramos, J.D. (1990) PLV: programa de control y análisis del difractómetro de rayos X. Deposito legal M-11719, Granada, Spain.

Mazzucato, E., Artioli, G., and Gualtieri, A. (1999) High temperature dehydroxylation of muscovite-$2M_1$: a kinetic study by in situ XRPD. Physics and Chemistry of Minerals, 26, 375–381.

Mellini, M. and Menechini, R. (1985) Proportionality factors for the thin film TEM/EDS microanalysis of silicate minerals. Rendiconti della Societá Italiana de Mineralogia e Petrologia, 40, 261–266.

Muan, A. (1957) Phase equilibria at liquidus temperatures in the system iron oxide-Al_2O_3-SiO_2 in air atmosphere. Journal of the American Ceramic Society, 40, 121–133.

Muan, A. and Osborn, E.F. (1965) Phase equilibria among oxides in steelmaking. Addison-Wesley, Reading, Massachusetts.

Mullin, J.W. (1992) Crystallization (3rd edition). Butterworth, London.

Osborn, E.F. and Muan, A. (1960) Phase equilibrium diagrams for ceramists. American Ceramic Society, Columbus, OH.

Pannhorst, W. and Schneider, H. (1978) The high-temperature transformation of andalusite (Al_2SiO_5) into 3/2-mullite ($3Al_2O_32SiO_2$) and vitreous silica (SiO_2). Mineralogical Magazine, 42, 195–198.

Peters, T. and Iberg, R. (1978) Mineralogical changes during firing of calcium-rich brick clays. Ceramic Bulletin, 57, 503–509.

Putnis, A. (1992) Introduction to mineral sciences. Cambridge University Press, U.K.

Rahman, S. and Weichert, H.T. (1990) Interpretation of HREM images of mullite. Acta Crystallographica, B46, 139–149.

Raterron, P., Carpenter, M., and Doukhan, J.C. (1999) Sillimanite mullitization: ATEM investigation and point defect model. Phase Transitions, 68, 481–500.

——— (2000) ATEM investigation of experimentally annealed sillimanite: new constraints for the SiO_2-Al_2O_3 join. Mineralogical Magazine, 64, 247–254.

Rehak, P., Kunath-Fandrel, G., Losso, P., Hildmann, B., Schneider, H., and Jäger, C. (1998) Study of the Al coordination in mullites with varying Al:Si ratio by ^{27}Al NMR spectroscopy and X-ray diffraction. American Mineralogist, 83, 1266–1276.

Roy, R. (1949) Decomposition and resynthesis of the micas. Journal of the American Ceramic Society, 32, 202–209.

Rubie, D.C. (1986) The catalysis of mineral reactions by water and restrictions on the presence of aqueous fluid during metamorphism. Mineralogical Magazine, 50, 399–415.

Rubie, D.C. and Brearley, A.J. (1987) Metastable melting during the breakdown of muscovite+quartz at 1 kbar. Bulletin Minéralogie, 110, 533–549.

Saalfeld, H. and Guse, W. (1981) Structure refinement of 3:2 mullite ($3Al_2O_3 \cdot 2SiO_2$). Neues Jahrbuch für Mineralogie Monatshefte, 4, 145–150.

Schairer, J.F. and Bowen, M.L. (1947) Melting relations in the systems Na_2O-Al_2O_3-SiO_2 and K_2O-Al_2O_3-SiO_2. American Journal of Science, 245, 193–204.

Sanchez-Navas, A. (1999) Sequential kinetics of a muscovite-out reaction: A natural example. American Mineralogist, 84, 1270–1286.

Schmücker, M., Schneider, H., Poorteman, M., Cambier, F., and Meinhold, R. (1995) Constitution of mullite glasses produced by ultra-rapid quenching of plasma-sprayed melts. Journal of the European Ceramic Society, 15, 1201–1205.

Schneider, H. and Pleger, R. (1993) The reconstructive 2/1- to 3/2-mullite transformation in the presence of Fe_2O_3-rich glass at 1570 °C. European Journal of Mineralogy, 5, 515–521.

Schneider, H., Okada K., and Pask, J. A. (1994) Mullite and mullite ceramics. John Wiley, Chichester.

Sunagawa, I. (1981) Characterization of crystal growth in nature as seen from the morphology of mineral crystals. Bulletin Mineralogie, 104, 81–87.

Sundius, N. and Byström, A.M. (1953) Decomposition products of muscovite at temperatures between 1000 °C and 1260 °C. Transactions of the British Ceramic Society, 52, 632–642.

Tiller, W.A. (1991) The science of crystallization: Microscopic interfacial phenomena. Cambridge University Press, U.K.

Tite, M.S. and Maniatis, Y. (1975) Examination of ancient pottery using the scanning electron microscope. Nature, 257, 123–123.

Udagawa, S., Urabe, K., and Hasu, H. (1974) The crystal structure of muscovite dehydroxylate. Japanese Association of Mineralogists, Petrologists and Economic Geologists, 69, 381–389.

Vassányi, I. and Szabó, A. (1993) Thermic dehydroxylation of muscovite-$2M_1$. Materials Science Forum, 133–136, 655–658.

Velde, B. (1966) Upper stability of muscovite. American Mineralogist, 51, 924–929.

Worden, R.H., Champness, P.E., and Droop, G.T.R. (1987) Transmission electron microscopy of pyrometamorphic breakdown of phengite and chlorite. Mineralogical Magazine, 51, 107–121.

MANUSCRIPT RECEIVED APRIL 23, 2002
MANUSCRIPT ACCEPTED NOVEMBER 8, 2002
MANUSCRIPT HANDLED BY ADRIAN BREARLEY